Acta Cryst B
STRUCTURAL SCIENCE
CRYSTAL ENGINEERING
MATERIALS

ISSN 2052-5206

Two rhodamine 6G derivative compounds: a structural and fluorescence single-crystal study

Matias Di Paolo,[a] Mariano L. Bossi,[a] Ricardo Baggio[b] and Sebastián A. Suarez[a,b]*

[a]Departamento de Química Inorgánica, Analítica y Química Física, Facultad de Ciencias Exactas y Naturales, Universidad de Buenos Aires, Ciudad Universitaria, Pab. II (1428), Buenos Aires, Argentina, and [b]Gerencia de Investigación y Aplicaciones, Centro Atómico Constituyentes, Comisión Nacional de Energía Atómica, Buenos Aires, Argentina. *Correspondence e-mail: seba@qi.fcen.uba.ar

Received 17 March 2016
Accepted 8 June 2016

Edited by E. V. Boldyreva, Russian Academy of Sciences, Russia

Keywords: rhodamine 6G derivatives; photocrystallography; fluorescence; weak interactions; atoms in molecules theory.

CCDC references: 1484174; 1484175

Supporting information: this article has supporting information at journals.iucr.org/b

The synthesis, characterization, structural analysis and fluorescence properties of two rhodamine 6G derivatives are described, namely a propargylamine derivative, 3′,6′-bis(ethylamino)-2′,7′-dimethyl-2-(methylcyanide)spiro[isoindole-1,9′-xanthen]-3(2*H*)-one (I), and a γ-aminobutyric acid (GABA) derivative, 3′,6′-bis(ethylamino)-2′,7′-dimethyl-3-oxospiro[isoindole-1,9′-xanthen]-2(3*H*)-yl)butyricacid (II). Both structures are compared with four similar ones from the Cambridge Structural Database (CSD), and the interactions involved in the stabilization are analyzed using the atoms in molecules (AIM) theory. Finally, a single-crystal *in-situ* reaction study is presented, carried out by fluorescence methods, which enabled the 'opening' of the spirolactam ring in the solid phase.

1. Introduction

Photochromism in a reversible transformation consists of a chemical species between two isomeric forms with different absorption spectra. The changes involved may be produced in just one or both directions by photoirradiation (Irie *et al.*, 2014). The importance of compounds presenting photochromism resides in the fact that the changes produced in the chemical bonds may result in electronic modifications as well as in changes in the geometrical structure of the molecule. This possibility to modify their electronic structure makes them potentially useful materials for the design of optical memory media and photoswitch devices. In addition, changes in the geometric structure can be applied to the manufacture of light-driven actuators, *inter alia* (Irie, 1994; McArdle, 1992). In all these aforementioned applications thermal irreversibility is an essential and indispensable property for the photosensitive molecules in order to be useful (Irie *et al.*, 2014). Although a large number of photochromic molecules have been reported, those presenting a photochromic reaction in the *crystalline phase* are rare, such as diarylethene (Kobatake *et al.*, 1999; Irie *et al.*, 2014).

Consequently, an extremely interesting family of compounds usually analyzed in the solid state by means of photocrystallography techniques is spirorhodamines. Possible mechanisms for crystalline photochromism are the reversible formation of radicals or hydrogen transfer (Irie *et al.*, 2000; Xu *et al.*, 2016; Bergmann *et al.*, 2002), as occurs with spirorhodamines in solution. These xanthenic colourants are an amide-derivatives subgroup of rhodamine (Bossi *et al.*, 2008; Montenegro *et al.*, 2012) with the characteristic that their emission properties can be modulated by changing the identity of the substituents in the amino group, a fact which may result

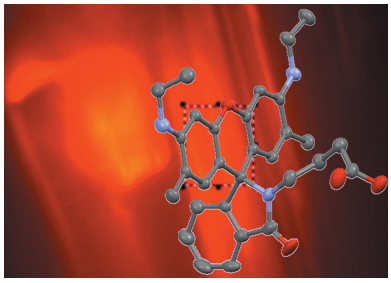

in changes of maximum absorption and emission wavelength or fluorescence quantum yield (Adamczyk & Grote, 2000). The photochromic transformation of these compounds involves bond breaking/formation (Fig. 1). The 'closed' isomer (*a*) only absorbs light in the UV range and does not present fluorescence emission, while the 'open' zwitterion (*b*) has high fluorescence quantum yields. The shift to the open form occurs photochemically, whereas its closure is a thermally driven reaction, with a kinetic constant (K_{Δ}) depending strongly on the *environment*: for example, K_{Δ} is of the order of milliseconds in polar solvents, but it is in the order of hours in polyvinyl alcohol (Fölling *et al.*, 2007).

In the present work we describe two rhodamine 6G derivatives, composed of a substituted 2′,3′,6′,7′-xanthene group (hereinafter *xant*) and a 3*H*-indole-3one (hereinafter *ind*; Scheme 1) *viz*. the propargylamine derivative 3′,6′-bis(ethylamino)-2′,7′-dimethyl-2-(methylcyanide)spiro[isoindole-1,9′-xanthen]-3(2*H*)-one (I) and the γ-aminobutyric acid derivative 3′,6′-bis(ethylamino)-2′,7′-dimethyl-3-oxospiro[isoindole-1,9′-xanthen]-2(3*H*)-yl)butyric acid (II). Their synthesis, chemical characterization and X-ray crystal structure determination are presented. In order to determine the nature and relative strengths of the intermolecular interactions present in both structures, a topological analysis in the framework of Bader's 'atoms in molecules' (AIM) theory (Bader, 1990) has been applied. Finally, the result of an *in situ, single-crystal fluorescence experiment* is shown, in which the rupture of the spirolactam ring in the single crystals could be clearly followed, a phenomenon seldom reported in the solid state.

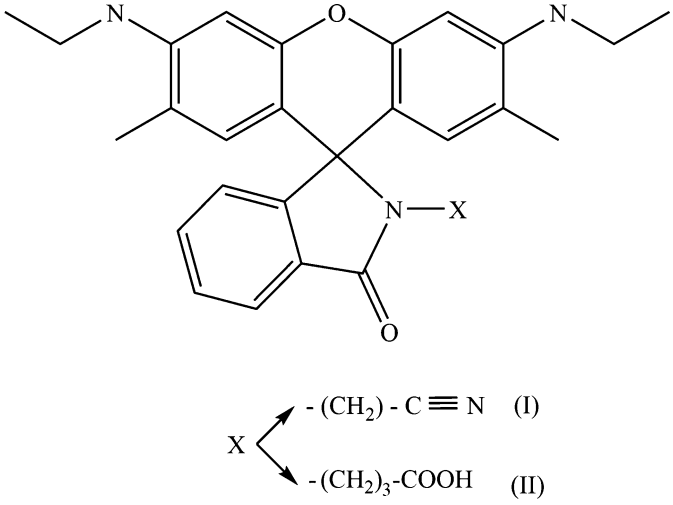

(III): H; (IV): NH - CH_2 - CH_2OH;
(V): N = CH - CH_2-CH_3; (VI): N = CH - CH = O

Scheme 1

2. Experimental

An Exeter Analytical CE-440 elemental analyser was used for microanalysis (C, H, N). NMR spectra were recorded on a Bruker AM 500 MHz. Electrospray ionization (ESI) mass spectra were measured on a Bruker micrOTOF-Q II. Single-crystal X-ray diffraction data were collected using a Gemini diffractometer (Oxford Diffraction). Measurements were performed at 170 K with a Desktop cooler (Oxford Cryosystems). Data collection strategy and data reduction followed standard procedures implemented in *CrysAlisPro* software (Oxford Diffraction, 2009).

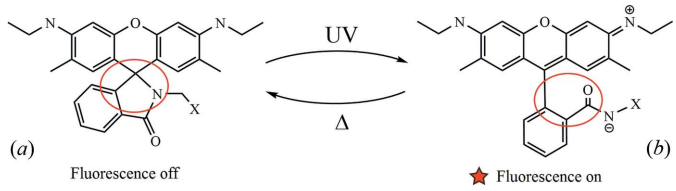

Figure 1
Photochromic transformation of rhodamine 6G derivatives.

Steady-state absorption and fluorescence spectra, as well as kinetic measurements with either absorption or fluorescence emission detection, were performed in a Shimadzu UV–visible spectrophotometer model UV-1603 or in a PTI Quantamaster fluorescence spectrofluorometer. In Fig. 2, the experimental set-up used for the single-crystal absorption and fluorescence analysis of the compounds is shown. Briefly, the setup is a homemade wide-field microscope composed of two irradiation sources, a 532 nm CWDPSS laser (SDL- 532-200T; Shanghai Dream Lasers Technology) and a 355 nm CWDPSS laser (UVL-355-10, LaserLabComponents Inc.), combined by means of a dichroic mirror (DCLP 425, AHF analysen technik AG) and focused with an achromat lens (f200) onto the back focal plane of the objective lens (Leica PLAN 100x, 1.25 NA, oil immersion), to achieve wide-field illumination. Fluorescence emission was collected by the same objective, separated from the excitation sources with a dichroic mirror (Z488-532rpc, Chroma Technology), selected with a bandpass filter

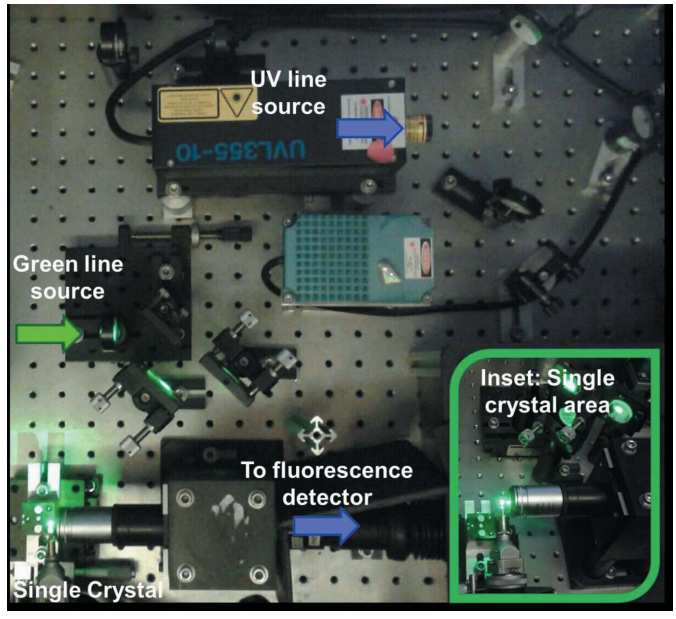

Figure 2
Single-crystal absorption and fluorescence measurement setup.

(HQ580/40, AHF analysentechnik AG), and focused in the detector, an EMCCD camera (IXON-DU-897; Andor Technology)

2.1. Synthesis and crystallization

The two photocromic rhodamine derivatives (I) and (II) were synthesized using commercial rhodamine 6G as a starting product and performing amidation reactions as reported by Beija *et al.* (2009). Both syntheses were carried out using DMF as an aprotic polar solvent in the presence of catalytic amounts of TEA (triethylenediamine), an organic base which inhibits the reversibility of the reaction, and allows the electron pair of the amine N to be readily available. A 1:3 molar ratio between rhodamine 6G and the derivative with an amino-terminal group was used, in order to obtain the spiro-rhodamine (SRA). The reaction mixture was stirred at room temperature for 24 h, and followed by thin-layer chromatography until the disappearance of the reactant signals. After 24 h the solution was placed in a water/ice bath where the formation of a red precipitate was almost immediately observed. The purification was carried out by dissolution and re-precipitation cycles with methanol in a water/ice bath. The purity of the products obtained was finally assessed by their NMR spectra (Fig. 3).

Regarding crystallization, in the case of (I) it was performed dissolving the CN derivative compound in a 3:2 acetone/methanol mixture. The top of the containing vial was pierced with a hypodermic needle and the mixture was left in the refrigerator over a week. In the case of (II) the powder sample was dissolved in a 3:2:1 acetone:methanol:ethanol mixture and left concentrating at room temperature for about 2 weeks.

In both cases well formed orange crystals were obtained, further separated by filtration and washed with diethyl ether (3 × 5 ml; yield: 50–60%). For (I), ESI-MS (MeOH) *m*/*z* 451.2118 [*M*+H]+ (calc. 451.2134). Anal: calc. for $C_{28}H_{26}N_4O_2$: C 74.6, H 5.8, N 12.4%; found: C 74.8, H 5.9, N 12.4%. For (II), ESI-MS (MeOH) *m*/*z* 500.2548 [*M*+H]+ (calc. 500.2549). Anal: calc. for $C_{30}H_{33}N_3O_4$: C 72.1, H 6.6, N 8.4%; found: C 71.9, H 6.6, N 8.3%.

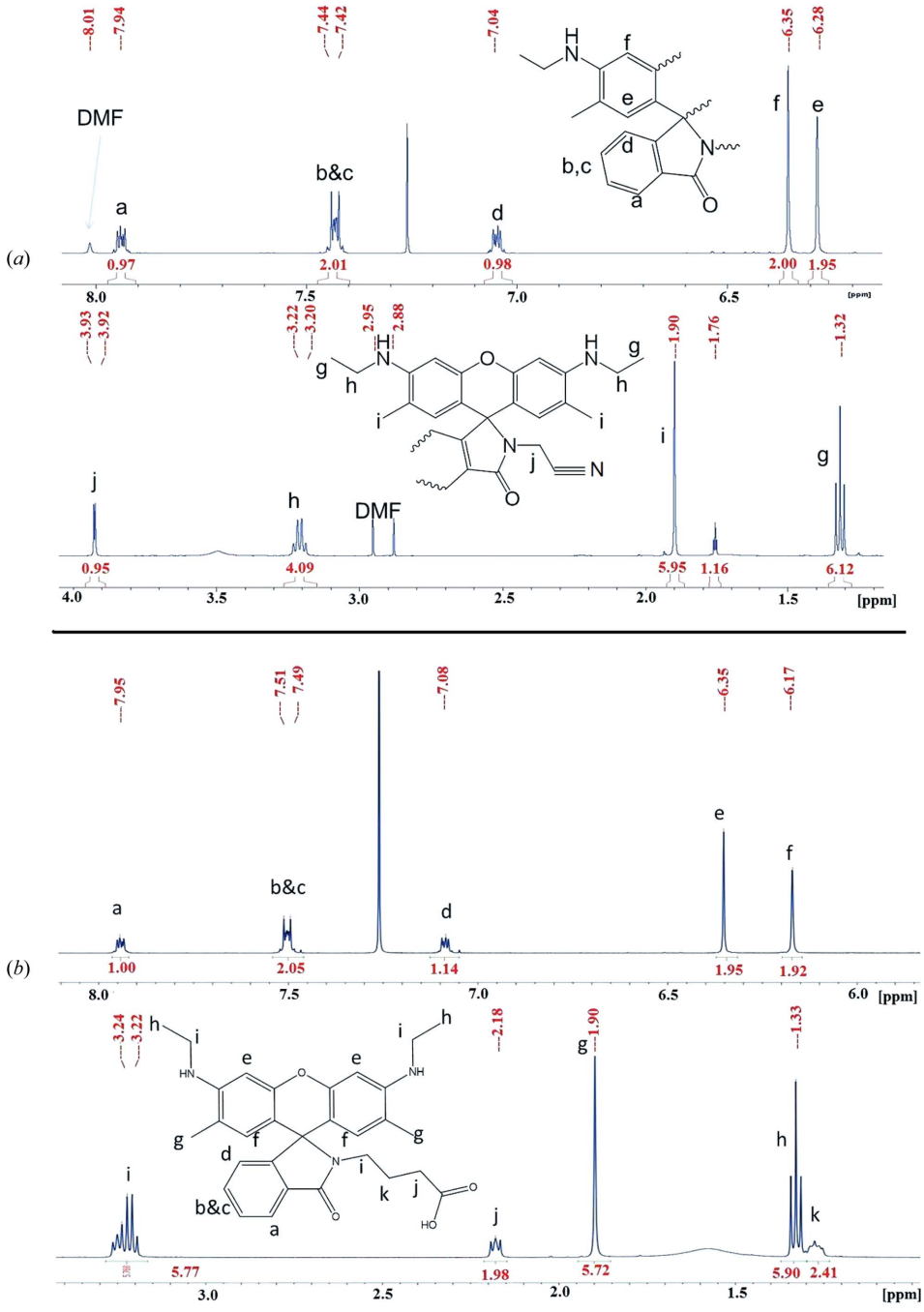

Figure 3
NMR spectra of both rhodamine 6G derivatives. (*a*) CN (I); (*b*): GABA (II).

2.2. Crystal structure resolution and refinement

The crystal structures were solved by direct methods (*SHELXS97*; Sheldrick, 2008) and refined by least squares on F^2 (*SHELXL*2014/6, Sheldrick, 2015).

All H atoms were identified in an intermediate difference map and were refined with different constraints according to their environment. H atoms on C atoms were idealized and allowed to ride

Table 1
Experimental details.

For all structrures: triclinic, $P\overline{1}$, $Z = 2$. Experiments were carried out at 170 K with Mo $K\alpha$ radiation using an Oxford Diffraction Gemini CCD S Ultra. Absorption was corrected for by multi-scan methods, *CrysAlisPro*.

	(I)	(II)
Crystal data		
Chemical formula	$C_{28}H_{26}N_4O_2$	$C_{30}H_{33}N_3O_4$
M_r	450.53	499.59
a, b, c (Å)	8.9389 (5), 9.7292 (7), 16.0650 (8)	9.4250 (6), 11.6209 (4), 12.6080 (5)
α, β, γ (°)	89.067 (5), 78.856 (4), 62.927 (6)	88.708 (3), 68.696 (5), 86.313 (4)
V (Å^3)	1216.48 (14)	1283.89 (11)
μ (mm^{-1})	0.08	0.09
Crystal size (mm)	0.50 × 0.40 × 0.35	0.30 × 0.20 × 0.20
Data collection		
T_{min}, T_{max}	0.94, 0.98	0.97, 0.99
No. of measured, independent and observed [$I > 2\sigma(I)$] reflections	18 456, 5811, 3610	19 816, 6120, 3882
R_{int}	0.042	0.046
(sin $\theta/\lambda)_{max}$ (Å^{-1})	0.688	0.686
Refinement		
$R[F^2 > 2\sigma(F^2)]$, $wR(F^2)$, S	0.065, 0.203, 0.91	0.060, 0.171, 1.04
No. of reflections	5811	6120
No. of parameters	331	350
No. of restraints	6	2
H-atom treatment	H-atom parameters constrained	H atoms treated by a mixture of independent and constrained refinement
$\Delta\rho_{max}$, $\Delta\rho_{min}$ (e Å^{-3})	0.37, −0.26	0.31, −0.29

Table 2
Conformational parameters of the common fraction in all six structures (°).

Column: Mpln(xanth): mean deviation from the least-squares plane in the xanthenes groups; Ang(planes): angles subtended by the isoindole and xanthene least-squares planes. Ang(line): angle defined by the isoindole (pseudosymmetry) axis and the normal to the xanthene least squares plane.

#	Mpln(xant) (°)	Ang(planes) (°)	Ang(line) (°)
(I)	0.1254	90.3	7.7
(II)	0.0331	91.2	27.1
(III)	0.0631	90.0	19.8
(IV)	0.036	95.1	18.6
(V)	0.0833	90.0	9.2
(VI)	0.1767	90.0	7.4

both in coordinates and in displacement parameters, the latter taken as $U_{iso}(H) = xU_{eq}(C)$, with C—H = 0.93 Å and $x = 1.2$ for aromatic, C—H = 0.97 Å and $x = 1.2$ for methylene and C—H = 0.96 Å and $x = 1.5$ for methyl groups. H atoms attached to N and O were refined freely. One of the N-ethyl groups in (I) appeared disordered around the N—C bond and was modeled as two independent groups, with final occupancies of 68:32.

3. Molecular calculations

3.1. AIM: brief theoretical background

The quantum theory of atoms in molecules (AIM; Bader, 1990, 1991) provides an approach to the analysis of the electron density distribution of a molecule, an experimental observable, based on its topology. The magnitudes of the density at the critical points gives a measure of bond order and interaction strength and can be used to assess, at least in comparative terms, the real significance of some non-covalent interactions, usually evaluated only on geometrical grounds.

According to this theory, the structure of a many-electron system with a given nuclear configuration R is completely determined by a set and types of critical points of the charge density $\rho(r,R)$ where the gradient of the charge density vanishes [$\nabla\rho(r) = 0$]. The second derivatives of $\rho(r)$ calculated at these points comprise a real symmetrical Hessian matrix and the eigenvalues of the Hessian determine the type of critical point (Bader, 1990).

3.2. Programs used and approximations performed

Quantum-mechanical calculations on the complexes included in this study were performed at the PBEPBE-D/6-311++G(d,p) level of theory using the crystallographic coordinates (single point calculations) within the *GAUSSIAN*09 program (Frisch *et al.*, 2009). This level of theory includes the available dispersion correction (D3) and diffuse functions in the basis set and is adequate for studying non-covalent interactions dominated by dispersion effects, like, for instance, π-stacking (Foi *et al.*, 2014; Wang *et al.*, 2016). The basis set superposition error for the calculation of interaction energies on the dimers was corrected using the counterpoise method (estimated relative error for the energies < 5%).

The AIM analysis of the electron density has been performed at the same level of theory using the *Multiwfn* program (Lu & Chen, 2012). The Hirshfeld surfaces, mapped with d_{norm}, and two-dimensional fingerprint plots were generated using *CrystalExplorer*3.1 (Wolff *et al.*, 2012).

4. Results and discussion

4.1. Crystal structure

Crystal data, data collection and structure refinement details are summarized in Table 1.

Both compounds (I) and (II) are rhodamine 6G derivatives composed of a substituted 2′,3′,6′,7′-xanthene group and a 3*H*-indole-3-one at N, as shown in Scheme 1 and Fig. 4. They crystallize in the triclinic space group $P\overline{1}$, with one single molecule in the asymmetric unit ($Z' = 1$), and their displacement ellipsoid plots with labeling schemes can be found in Figs. 5 and 6.

Bond distances and angles are inconspicuous and will not be discussed in detail here. In fact, the most interesting aspects of the structures reside in the particular way in which the different substituents affect non-covalent interactions, and how this latter fact shows up in the crystal structures, sometimes in a dramatic way.

For this purpose we shall compare (I) and (II) with each other, and with a group of related rhodamine 6G derivatives, already reported in the literature and presented in Scheme 1, *viz*. (III), X = H (Shangguan & Liu, 2004; Refcode AVIBIQ), (IV), X = NH—CH_2—CH_2OH (Tian & Peng, 2008), (V), X = N═CH—CH_2—CH_3 (Li *et al.*, 2013) and (VI), X = N═CH—CH═O (Li *et.al.*, 2009).

To appreciate the similarities and differences Fig. 4 shows a least-squares fit of the common fraction in all six structures (no pendant groups considered), where the complete three rings set in the xanthene group have been used for fitting.

It is apparent that all six structures share the main property of having the isoindole group almost perpendicular to the xanthene base (Fig. 4*a*; angular range: 90.0—95.1°, Table 2). However, the isoindole (pseudosymmetry) axis can deviate significantly from the normal to the xanthene plane (Fig. 4*b*; angular range: 7.4–27.1°).

Since structures (I) and (II) are precisely the ones which depart more severely in this latter comparison, we shall describe with some care the interactions in which they are involved, see Tables 3 (hydrogen bonding) and 4 ($\pi\cdots\pi$). The entries are identified by a code (first column) in such a way that those ending in 'a' refer to (I) while the ones ending in 'b' correspond to (II).

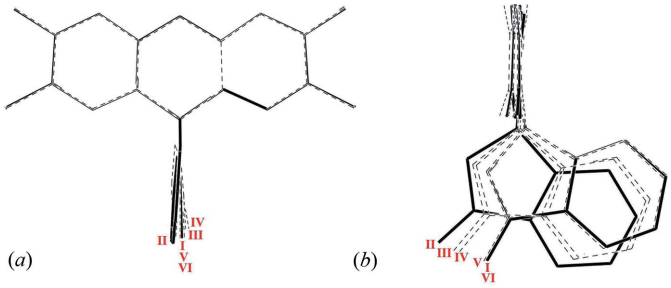

Figure 4
Least-squares fit of the isoindole group and xanthene base in all six structures.

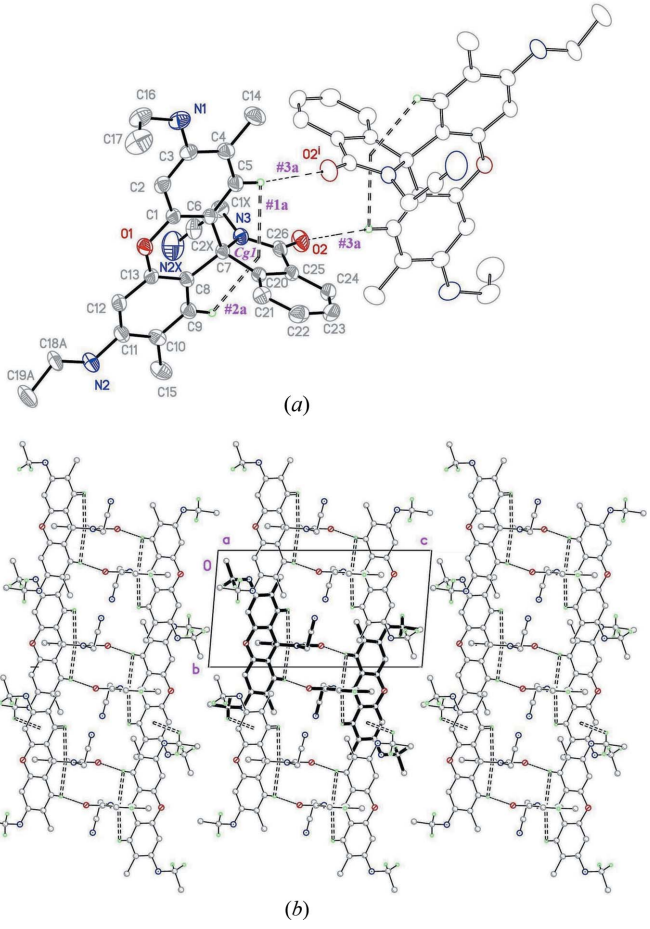

Figure 5
Intermolecular interactions in (I): (*a*) Dimeric unit, showing the labeling scheme used. Ellipsoid plots drawn at the 50% level. (*b*) Packing view along [100].

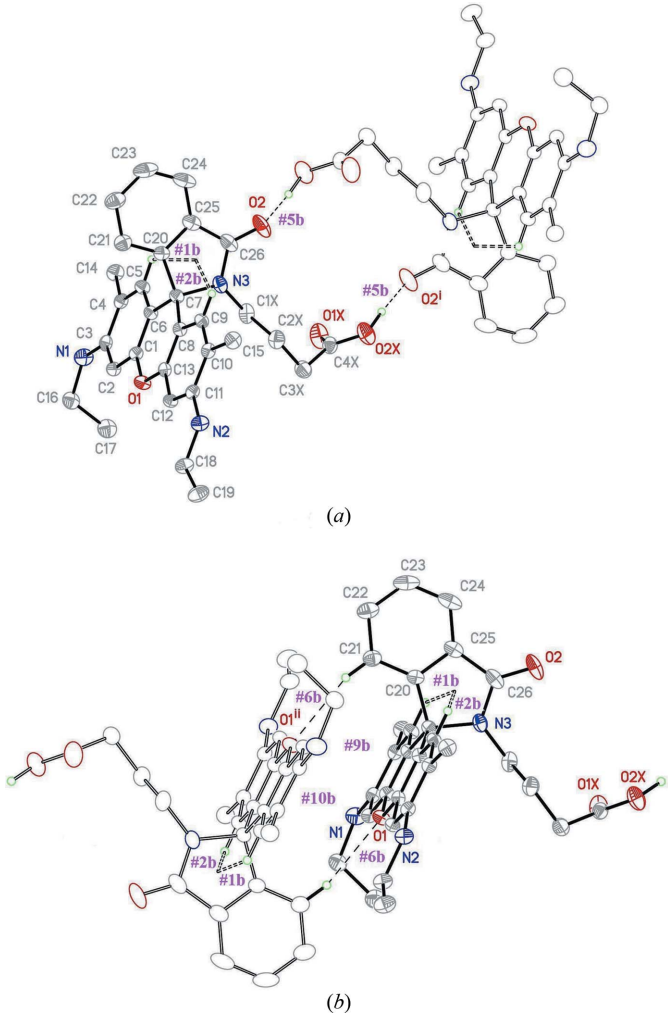

Figure 6
View of the two different dimeric entities in (II), showing the labeling scheme used. Ellipsoid plots are drawn at the 50% level.

Table 3
Hydrogen-bond geometry (Å, °) for (I) and (II).

Label	D—H···A	D—H (Å)	H···A (Å)	D···A (Å)	D—H···A (°)	Character	AIM results (a.u.)	
							$100 \times \rho$	$10 \times \nabla^2\rho$
(I)								
#1a	C5—H5···Cg1	0.93	2.70	2.993 (3)	99	Intramolec.	–	–
#2a	C9—H9···Cg1	0.93	2.69	2.988 (2)	100	Intramolec.	–	–
#3a	C5—H5···O2^{i}	0.93	2.47	3.394 (3)	170	Dimeric	0.80	0.28
#4a	C23—H23···Cg2^{ii}	0.93	2.92	3.796 (3)	157	Interdimer.	0.50	0.20
#5a	C16—H16*B*···Cg4^{iii}	0.97	2.87	3.524 (3)	126	Interdimer.	0.54	0.22
#6a	C18*B*—H18*C*···Cg3^{iv}	0.97	2.95	3.578 (13)	123	Interdimer.	0.53	0.21
(II)								
#1b	C5—H5···Cg1	0.93	2.63	2.945 (2)	100	Intramolec.	–	–
#2b	C9—H9···Cg1	0.93	2.72	3.020 (2)	99	Intramolec.	–	–
#3b	C1*X*—H1*XB*···Cg2	0.97	2.77	3.138 (2)	103	Intramolec.	0.70	0.23
#4b	C2*X*—H2*XA*···Cg4	0.97	2.98	3.837 (2)	148	Intramolec.	0.70	0.23
#5b	O2*X*—H2*X*···O2^{i}	1.09 (5)	1.52 (5)	2.591 (2)	170 (4)	Dimeric (*A*)	6.40	1.61
#6b	C21—H21···O1^{ii}	0.93	2.57	3.473 (3)	165	Dimeric (*B*)	0.71	0.24
#7b	N1—H1N···O1*X*^{iii}	0.83 (3)	2.49 (3)	3.245 (3)	153 (2)	Intercolumn.	0.94	0.29
#8b	N2—H2N···O1*X*^{iv}	0.85 (2)	2.46 (2)	3.267 (2)	158 (2)	Intercolumn.	0.95	0.29

General ring codes (both structures): Cg1: N3,C7,C20,C25,C26; Cg2: O1,C1,C6,C7,C8,C13; Cg3: C1,C2,C3,C4,C5,C6; Cg4: C8,C9,C10,C11,C12,C13; Cg5: C20,C21,C22,C23,C24,C25. Symmetry codes: Structure (I): (i) $-1-x, 2-y, 1-z$; (ii) $-1+x, y, z$; (iii) $x, 1+y, z$; (iv) $1+x, -1+y, z$. Structure (II): (i) $1-x, -y, -z$; (ii) $-x, 1-y, 1-z$; (iii) $-x, -y, 1-z$; (iv) $x, 1+y, z$.

Regarding intramolecular interactions, the C—H···π ones at both sides of the spirolactam ring (#1a, #2a and #1b, #1b) are a common feature of both structures, as well as for all the remaining ones in the group, and have some relevance in the 'pseudo-mirror' symmetry shown by the naked groups in Fig. 4. In addition, structure (II) presents a couple more (#3b, #4b) in which methylene H's of the organic acid are involved.

However, the really interesting structural features are determined by the intermolecular interactions. The case of (I) is simpler to describe. Even if all these intermolecular interactions are weak, there is a leading one (#3a) which defines a centrosymmetic dimer through an $R_2^2(14)$ loop (Fig. 5*a*). These dimers are in turn interlinked by three different C—H···π contacts (#4a to #6a) which connect them along *a* and *b*, to define planes parallel to (001) (Fig. 5*b*). In the case of (II) things are more interesting: there are two dimeric entities determined by interactions of quite different nature, shown in Fig. 6. The first one (Fig. 6*a*) is the result of a very strong O—H···O bond (#5a), the strength of which will be confirmed later by some AIM calculations, but for the time being it will suffice to note that the central H (freely refined) moves significantly away from the O donor, towards the acceptor [1.09 (5) Å:1.52 (5) Å]. As a result an $R_2^2(18)$ loop builds up, connecting the centrosymmetrically related moieties. The second dimer (Fig. 6*b*) results from the collective effect of a number of

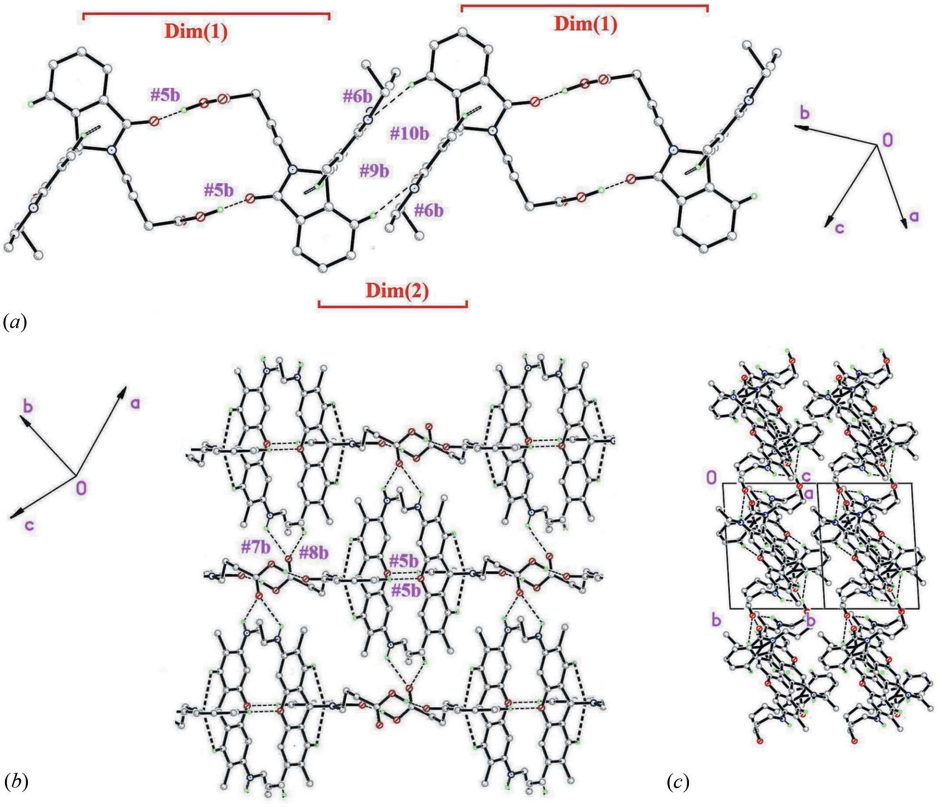

Figure 7
Substructures derived from the different dimeric entities in (II). (*a*) Columns along [$\bar{1}$11] defined by dimeric groups. (*b*) Planar arrays parallel to (101) in a view perpendicular to the planes. (*c*) Packing view at right angles to the latter, with planes displayed sideways and showing the rather weak interaction between them.

Table 4
π–π contacts (Å, °) for (II).

Label	Cg···Cg	ccd (Å)	da (°)	sa (°)	ipd (Å)	Character	AIM results (a.u.)	
							$100 \times \rho$	$10 \times \nabla^2\rho$
(II)								
#9b	Cg2···Cg2^{ii}	3.9989 (11)	0	33.4	3.3402 (8)	Dimeric (*B*)	0.58	0.16
#10*b*	Cg3···Cg4^{ii}	3.8820 (11)	2.33 (9)	29.2 (10)	3.3541 (8)	Dimeric (*B*)	0.58	0.16

ccd: centre-to-centre distance; da: dihedral angle between planes, sa: slippage angle (average angle subtended by the intercentroid vector to the plane normal), ipd: interplanar distance (average distance from one plane to the neighbouring centroid). For details, see Janiak (2000). Symmetry codes: structure (II): (ii) $-x, 1-y$

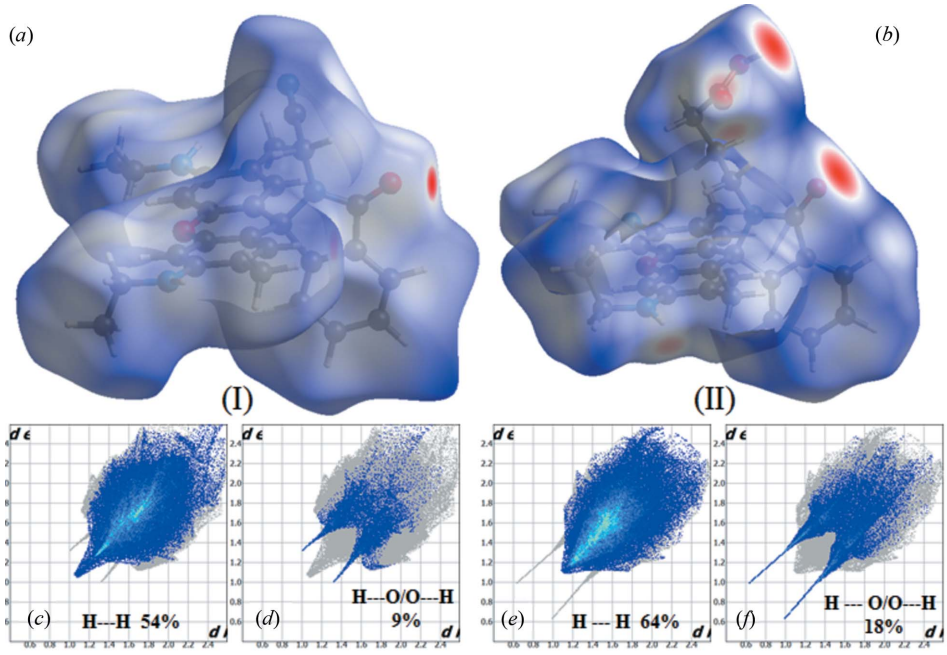

Figure 8
Hirshfield surfaced mapped with d_{norm} for (*a*) (I) and (*b*) (II). The surfaces are shown as transparent to allow visualization of the molecular moiety. (*c*)–(*f*) Fingerprint plots resolved into H···H and O···H/H···O contacts for (I) and (II).

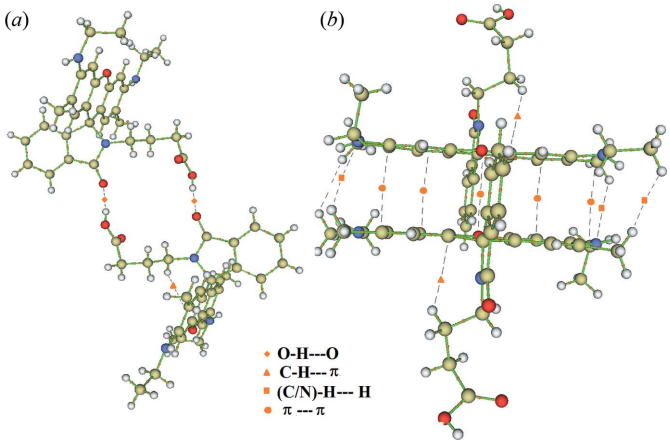

Figure 9
Left: dimer *A*; right: dimer *B*. In orange, selected 'bond critical points' for (II) are shown: diamonds: O—H---O; triangles: C—H---π; squares: (C/N)—H—H; dots: π---π. The bond paths are shown in the dotted line.

C—H···O (#6b) and π···π (#9b, #10b) interactions which, even if individually too weak as to be of any significance, collectively can rival with the former O—H···O in magnitude (as shown below).

The concatenation of these dimeric groups define columns along [$\bar{1}$11] (Fig. 7*a*), further interconnected by N—H···O bonds (#7b, #8b) to define planar arrays parallel to (101) (Fig. 7*b*) only slightly interacting with each other (Fig. 7*c*).

Before going into a quantitative analysis of the relative interaction strengths it is perhaps worth discussing in qualitative terms the differences which (I) and (II) end up showing as a result of the different substituents, $X_{(I)}$ = (CH_2)—C≡N; $X_{(II)}$ = $(CH_2)_3$—COOH. An intriguing feature is why compound (I) does not show any π···π bonding interaction, while the same aromatic nucleus generates an extremely strong one in (II). The reason seems to rely on the absence [in (I)] or presence [in (II)] of the interactive carboxylate OH, and the strong O—H···O bond it gives rise to. The effect in (II) is to drag the *ind* group away from the *xant* base [compound (II) shows the *largest* departure of the *ind* axis away from the normal to the *xant* plane; Table 2] leaving the large planar group prone to an approach by a similar centrosymmetric moiety. At the same time, the intercolumnar N—H···O bonds #7b, #8b drag the bulky terminal CH_2CH_3 groups away, thus allowing for the relative approach of neighbouring *xant* groups and, concomitantly, the building of π···π bonds #9b, #10b. In the case of (I), all these favourable circumstances are absent: the much weaker dimeric C—H···O bond #3a is not adequately directed nor has the required strength as to drag the *ind* group away [compound (I) shows the *smallest* departure of the *ind* axis away from the normal to the *xant* plane; Table 2]. Contrasting with (II), the terminal N—CH_2CH_3 group in (I) is not dragged away by way of hydrogen bonds, its

bulky presence concomitantly hampering any possible interactive approach of *xant* groups.

A graphical picture of the above regarding the relevance of the interactions is provided by the Hirshfeld surface of both molecular moieties, as illustrated in Figs. 8(*a*) and (*b*) showing the surfaces that have been mapped over d_{norm}. The largest interactiveness in (II) is apparent.

4.2. Atoms in molecules analysis

In order to compare the interactions described so far we have made use of Bader's theory of atoms in molecules (AIM; Bader, 1990). In particular, we were interested in the driving forces leading to the formation of both dimeric units in (II). At this stage it is perhaps relevant to state that the theory predicts four different types of critical points (bond, ring, cage, nuclear), but in the present case only 'bond type' points are pertinent and will be the ones to be discussed. The results, in the form of the distribution of bond critical points (BCP) for (II), are shown in Figs. 9(*a*) and (*b*), with different symbols for different critical points, while individual values for the Laplacian (determined as the sum of the eigenvalues of the Hessian of the electron density) and the electron density itself (both calculated at the critical points) can be found as the two final columns in Tables 3 and 4 (as usual in this type of calculation, values are relative and expressed in arbitrary units, a.u.). As analyzed in the original paper by Bader (1991) these magnitudes of the density can be used as a measure of bond order and interaction strength.

As expected, the largest value for $\nabla^2\rho$ was obtained for the dimeric O—H—O hydrogen bond #5b in (II) (dimer *A*). Inspection of Tables 3 and 4 confirms the weak character of all the remaining interactions, with rather small values for (ρ) and ($\nabla^2\rho$) at the BCP comparable to those reported for similarly weak intermolecular hydrogen bonds (Koch & Popelier, 1995; Geith *et al.*, 2005; Shahi & Arunan, 2014; Wang *et al.*, 2016). However, when taken in association, the large number of attractive intermolecular contacts defining dimer *B* determine in (II) an overall interaction [as defined by the sum of the (ρ) values at the BCP] in the same order as that in dimer *A*: 12.8 for *A* (2* × #5b), with only 2 BCP, and 6.4 for B, where 9 BCP are involved (both values in a.u.). Although not surprising, this confirms that even in situations where one type of interaction is extremely favoured, the associated synergistic effect of a number of weaker interactions can be as stabilizing as the favoured one.

4.3. Fluorescence single-crystal study

The fluorescence properties being the main appeal of these compounds points towards a fluorescence study on single crystals which appeared as an obvious follow-up, with the analysis being undertaken on the same crystals used for the structure determination (the experimental set up used has already been described in §2, Fig. 2). Both compounds provided quite similar results, so only those for (II) have been discussed in detail here.

As a first step the spectrum was measured in solution (both in their 'closed' and 'open' state, Fig. 10*a*) in order to determine the appropriate wavelengths to be used. After that, the single crystals were positioned in the focal point of both lasers (UV and green) and then were initially irradiated with a green light in order to obtain a reference value (since the 'closed' isomer does not have fluorescence emission). At this stage irradiation with the UV laser was started, giving rise to the reaction described in Fig. 1, with the concomitant rupture of the spirolactam ring and with it, the corresponding fluorescence emission of the 'open' isomer. The final outcome can be clearly seen in Fig. 10(*b*). Even if this effect is fairly standard

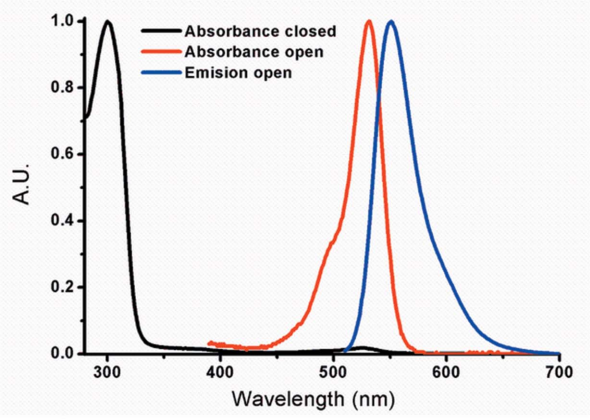

(*a*)

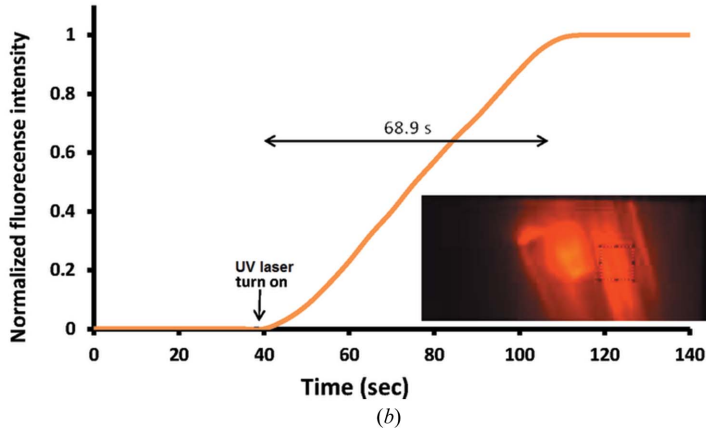

(*b*)

Figure 10
(*a*) Absorption spectrum in buffer (pH 2):ethanol (1:1) of the 'closed' (black, 301 nm) and 'open' (red, 531 nm) isomer for (II). In blue, the fluorescence emission spectra of the 'open' form (551 nm) (the 'closed' one does not have fluorescence emission). (*b*) Fluorescence signal of a single crystal of compound (II) measured in a wide-field microscope during the course of the photoisomerization induced with UV light (355 nm). The excitation laser (532 nm) was on during the whole experiment and the UV laser (355 nm) was switched on after 40 s; detection was selected with a band-pass filter of 580/40 nm. The acquisition frequency (frame rate) was 0.1 s, and the intensity of the sources was 1 mW (355 nm) and 120 mW (532 nm), measured at the back focal plane of the objective lens. In the inset, the last frame (wide-field image of the crystal) of the series is shown. A dotted square shows the area where the signal was integrated over time.

for rhodamines in solution, to our knowledge it has seldom been reported in the solid state.

5. Final remarks

At this stage a few words regarding the present and future are probably needed. The final emission of the irradiated compound, shown in Fig. 10(*b*), is irrefutable proof that at this stage the material was in its 'open' form. The obvious 'cherry on the cake' would have been to collect diffraction data on these crystals, at this very stage, in order to corroborate the assertion. However, transferring (or even mimicking) the fluorescence set up shown in Fig. 2 to the single-crystal diffractometer represents a paramount task, which, even if not discarded, we have been forced to postpone. An alternative way of obtaining single crystals of the 'open' form would have been generating them directly from a solution with an adequate pH so as to ensure the 'open' state of the molecule (Montenegro *et al.*, 2012). Since the kinetic constant (K_{Δ}) depends strongly on the environment there is a chance that the 'open' form in the solid state may be more stable. Unfortunately, even if a number of attempts on this line are on their way, for the time being they have proved to be unsuccessful

Our purpose is to continue to strive in this line of research, since we are confident that the outstanding performance shown by spirorhodamines in the single-crystal phase offers a great potential for future advances in optics and optoelectronic technologies.

Acknowledgements

The authors acknowledge Universidad de Buenos Aires, Comisión Nacional de Energía Atómica, and CONICET for research fellowships. We also acknowledge ANPCyT (project No. PME 2006–01113) for the purchase of the Oxford Gemini CCD diffractometer. Finally, the authors are grateful to Lic. Lucia Alvarez and Dra. Beatriz Araoz for their assistance with DFT analysis and fluorescence measurement, respectively.

References

Adamczyk, M. & Grote, J. (2000). *Bioorg. Med. Chem. Lett.* **10**, 1539–1541.
Bader, R. F. W. (1990). *Atoms in Molecules: A Quantum Theory.* Oxford University Press.
Bader, R. F. W. (1991). *Chem. Rev.* **91**, 893–928.
Beija, M., Afonso, C. A. M. & Martinho, J. M. G. (2009). *Chem. Soc. Rev.* **38**, 2410–2433.
Bergmann, U., Bendix, J., Glatzel, P., Gray, H. B. & Cramer, S. P. (2002). *J. Chem. Phys.* **116**, 2011–2015.
Bossi, M., Fölling, J., Belov, V. N., Boyarskiy, V. P., Medda, R., Egner, A., Eggeling, C., Schönle, A. & Hell, S. W. (2008). *Nano Lett.* **8**, 2463–2468.
Foi, A., Corrêa, R. S., Ellena, J., Doctorovich, F. & Di Salvo, F. (2014). *J. Mol. Struct.* **1059**, 1–7.
Fölling, J., Belov, V., Kunetsky, R., Medda, R., Schönle, A., Egner, A., Eggeling, C., Bossi, M. & Hell, S. W. (2007). *Angew. Chem. Int. Ed.* **46**, 6266–6270.
Frisch, M. J. *et al.* (2009). *GAUSSIAN*09. Gaussian Inc., Wallingford, Connecticut, USA.
Geith, J., Klapötke, T. M., Mayer, P., Schulz, A. & Weigand, J. J. (2005). *Acta Cryst.* C**61**, o545–o547.
Irie, M. (1994). *Photo-Reactive Materials for Ultrahigh-Density Optical Memory.* Elsevier: Amsterdam.
Irie, M., Fukaminato, T., Matsuda, K. & Kobatake, S. (2014). *Chem. Rev.* **114**, 12174–12277.
Irie, M., Lifka, T., Kobatake, S. & Kato, N. (2000). *J. Am. Chem. Soc.* **122**, 4871–4876.
Janiak, C. (2000). *J. Chem. Soc. Dalton Trans.* pp. 3885–3896.
Kobatake, S., Yamada, M., Yamada, T. & Irie, M. (1999). *J. Am. Chem. Soc.* **121**, 8450–8456.
Koch, U. & Popelier, P. L. A. (1995). *J. Phys. Chem.* **99**, 9747–9754.
Li, H., Cao, J., Zhu, H., Fan, J. & Peng, X. (2013). *Tetrahedron Lett.* **54**, 4357–4361.
Li, H., Fan, J., Wang, J., Tian, M., Du, J., Sun, S., Sun, P. & Peng, X. (2009). *Chem. Commun.* pp. 5904–5906.
Lu, T. & Chen, F. (2012). *J. Comput. Chem.* **33**, 580–592.
McArdle, C. B. (1992). *Applied Photochromic Polymer Systems.* Glasgow: Blackie.
Montenegro, H., Di Paolo, M., Capdevila, D., Aramendía, P. F. & Bossi, M. L. (2012). *Photochem. Photobiol. Sci.* **11**, 1081–1086.
Oxford Diffraction (2009). *CrysAlisPro*, Version 171.33.48. Oxford Diffraction Ltd, Abingdon, Oxfordshire, England.
Shahi, A. & Arunan, E. (2014). *Phys. Chem. Chem. Phys.* **16**, 22935–22952.
Shangguan, D. & Liu, G. (2004). Personal communication.
Sheldrick, G. M. (2008). *Acta Cryst.* A**64**, 112–122.
Sheldrick, G. M. (2015). *Acta Cryst.* C**71**, 3–8.
Tian, M.-Z. & Peng, X.-J. (2008). *Acta Cryst.* E**64**, o1645.
Wang, G., Chen, Z., Xu, Z., Wang, J., Yang, Y., Cai, T., Shi, J. & Zhu, W. (2016). *J. Phys. Chem. B*, **120**, 610–620.
Wolff, S. K., Grimwood, D. J., McKinnon, J. J., Turner, M. J., Jayatilaka, D. & Spackman, M. A. (2012). *CrystalExplorer*, Version 3.1. University of Western Australia, Australia.
Xu, B., Mu, Y., Mao, Z., Xie, Z., Wu, H., Zhang, Y., Jin, C., Chi, Z., Liu, S., Xu, J., Wu, Y.-C., Lu, P.-Y., Lien, A. & Bryce, M. R. (2016). *Chem. Sci.* **7**, 2201–2206.